Organic Microcrystal Array-Embedded Layer: Highly Directional Alternating *p*- and *n*-Channel for Ambipolar Transistor and Inverter

Minkyung Jea, Amit Kumar, Hyejin Cho, Dongmyung Yang, Hyunseok Shim, Akshaya K. Palai, Seungmoon Pyo*
Department of Chemistry, Konkuk University, 120 Neungdong-ro, Gwangjin-gu, Seoul 143-701, Republic of Korea.
E-mail: pyosm@konkuk.ac.kr

Abstract

An organic microcrystal array-embedded active layer for highly directional alternate *p*- and *n*-channel is prepared for fabricating a high-performance ambipolar organic field-effect transistor (OFET) and complementary inverter by successive depositions of *p*- and *n*-channel organic semiconductors on a polymeric gate dielectric. First, a microcrystal array of 6,13-bis(triisopropylsilylethynyl)pentacene (TIPS-pentacene, *p*-channel) is directly grown over the gate dielectric, and then a copper hexadecafluorophthalocyanine ($F_{16}CuPc$) layer is formed by a thermal evaporation method, resulting in the formation of an organic microcrystal array-embedded active layer with highly directional alternating *n*- and *p*-channels between the source and drain electrodes. Devices based on this active layer exhibited clear ambipolar charge transport characteristics with a high ambipolarity (> 90 %). The ambipolar charge transport mechanism is discussed in detail. In addition, air-stable complementary inverters comprising two ambipolar OFETs is also demonstrated.

Keywords: organic semiconductor; ambipolar organic field-effect transistors; inverters; polymer gate dielectric

Introduction

During the last few decades, organic semiconductors have attracted great interest because of their potential applications in large-area and low-cost molecular electronic devices [1-3] such as organic light-emitting diodes, organic field-effect transistors (OFETs), organic solar cells, and sensors. In addition to their low-cost and large-area coverage, these semiconductors offer a range of additional benefits, including ease of fabrication, low processing temperature, mechanical flexibility, and compatibility with plastic substrates, making this technology a viable alternative to amorphous silicon technology. [4] OFETs are of particular interest to the printed electronics industry with applications, including display devices, sensors, and electronic barcodes. [5] Most of the high-mobility organic semiconductors are predominantly unipolar OFETs based on hole (*p*-type) [6] or electron (*n*-type) [7] transport and their performance has almost reached the threshold for practical use. [8] There is also significant technological interest in fabricating devices such as inverters and light-emitting OFETs that require balanced charge transport behavior, [9] where both electron and hole transport are required. Inverters with unipolar transistors operate only in one quadrant (that is, either in the first or third). In contrast, ambipolar OFETs based on complimentary logic circuits allow operation in both (first and third) quadrants of transfer characteristics, thus providing a unique opportunity for achieving a high noise margin. [10] Crone *et al.* achieved complementary inverter circuits by separately performing the vacuum deposition of two *n*- and *p*-type semiconductor materials, which complicates the process of circuit fabrication. [11] Many groups have reported ambipolar OFETs based on organic semiconductors with various types of layer structures such as single component, [12] blend [13], and bilayer. [14] In 1995, Dodabalapur *et al.* [15] introduced an ambipolar OFET based on a C_{60}/α-hexathienylene (α-6T) organic heterojunction; thereafter, various heterojunctions such as C_{60}/pentacene, [16] CuPc/F_{16}CuPc, [17] BP_2T/F_{16}CuPc, [18] PTCDI-$C_{13}H_{27}$/pentacene, [19] and pentacene/ZnO [20] using well-known organic semiconductors such as pentacene, F_{16}CuPc, CuPc, and PTCDI derivatives were reported. Among these semiconductors, pentacene (*p*-type) and F_{16}CuPc (*n*-type) are well-studied materials for OFETs. [21] In addition, 6,13-bis(triisopropylsilylethynyl)pentacene (TIPS-pentacene), a solution-processable pentacene derivative,

has attracted much attention recently because of its good solubility in organic solvents and high hole mobility (1.73 cm^2/V·s).[22] Hence, a heterojunction of a solution-processable pentacene derivative (*p*-type) and F$_{16}$CuPc (*n*-type) is expected to afford high-performance ambipolar OFETs.

In our previous report, the *n*-channel TCNQ microcrystals based unipolar OFET devices were fabricated as a component of complimentary inverter circuitry with *p*-channel pentacene film based OFET.[23] In this work, we have incorporated the unipolar (*p*-type) micro-wires of TIPS-pentacene in *n*-type organic semiconductor material film (F$_{16}$CuPc) to obtain ambipolar charge transport by forming highly directional alternating *p*- and *n*-channels between the source and the drain. We also have analyzed the ambipolar OFETs and complementary inverter employing organic microcrystal array-embedded active layer and a with a solution-processable gate dielectric. The embedded active layer is composed of a highly ordered array of crystalline TIPS-pentacene prepared by solution processing and an air stable F$_{16}$CuPc thin film deposited directly on the TIPS-pentacene crystal array. In this device architecture, highly directional alternating *p*- and *n*-channels are formed between the source and the drain. This simple and efficient self-assembly method can be applied to the formation of large, elongated, and ordered crystalline arrays of other pi-conjugated organic molecules that can be employed to fabricate high-performance and low-cost ambipolar OFETs and inverters on polymer dielectrics. Devices based on this microcrystal embedded layer exhibited clear ambipolar charge transport characteristics with a high ambipolarity (> 90 %). The organic complementary inverter based on the ambipolar inverter exhibited efficient switching of the input voltage.

Results and discussion

In this study, three types of devices were fabricated. Fig. 1 shows a schematic of the unipolar organic field-effect transistors (Uni-OFETs) based on the (a) TIPS-pentacene microcrystal array, (b) F$_{16}$CuPc thin film, and (c) ambipolar organic field-effect transistors (Ambi-OFETs). The figure also shows the chemical structure of the compounds associated with the devices.

A schematic of the Ambi-OFET device and complementary inverter integrated with two Ambi-OFET devices is depicted in Fig. 2. TIPS-pentacene microcrystal array was grown by a unique solution-based approach previously reported by our group.[23] The method can be briefly described as follows: a capillary tube of outer diameter 1.2 mm was placed on the gate dielectric with its length parallel to the patterned-bottom indium-tin oxide (ITO) electrode. A solution of TIPS-pentacene in *o*-dichlorobenzene (0.1 wt%) was dropped on the tube [Fig. 2(a)]. The substrate was baked for 1 h on a hot plate at 90 °C under ambient conditions. The microwires formed as the solvent evaporated from the edges of the dropped solution [Fig. 2(b)]. The polarized optical microscope image of the as-formed crystal array is shown in Fig. 2(i), clearly demonstrating that the growth of the microwires is uniform and directional. The $F_{16}CuPc$ film is deposited on top of the crystal array [Fig. 2(c)], and finally, gold (Au) was deposited to complete the device [Fig. 2(d)]. The fabrication of the complementary inverter using the ambipolar OFETs is depicted in Fig. 2(e)-(h).

As components of the organic microcrystal array-embedded active layer, TIPS-pentacene and $F_{16}CuPc$ were used as *p*- and *n*-channel materials, respectively. We first have investigated the characteristics of uni-OFET devices based on microwires of TIPS-pentacene and $F_{16}CuPc$ thin-film on CL-PVP gate dielectric. For Uni-OFET based on microwires of TIPS-pentacene as shown in Fig. 3a, the polarized optical microscope image shows the long, highly ordered microwires of TIPS-pentacene are present between the source and drain electrodes. The as-formed crystal was confirmed by atomic force microscopy (AFM) (Fig. 3(b)). The height and width of the TIPS-pentacene wire are approximately 37 nm and 4 μm, respectively. The dimensions of the active channel of the OFET were measured from the OM and AFM images. The channel length (*L*) was measured to be 50 μm from the length of the shadow mask. The channel width (*W*) was determined to be 64 μm by measuring the contact area of the microwires crossing the source and drain electrodes. The output characteristics of the device measured at different gate biases (V_{GS}, varying from 0 to -40 V) with a step of -10 V show well defined *p*-type OFET characteristics and shown in supporting information (Fig. S1). The transfer characteristic curves (I_{DS} vs. V_{GS}) of the OFETs based on the TIPS-pentacene wires are depicted in Fig.

3(c). The corresponding output characteristic curves [drain current (I_{DS}) vs. drain voltage (V_{DS})] are depicted in the inset of Fig. 3(c). The output characteristics of the device measured at different gate biases (V_{GS}, varying from 0 to -80 V) with a step of -10 V show the typical *p*-type behavior. The maximum charge carrier mobility (μ_h) and the threshold voltage (V_{Th}) are calculated to be 7.2 x 10^{-1} cm^2/V·s and -15.7 V, respectively. This charge carrier mobility is much higher than those previously reported for solution-processed TIPS-pentacene OFETs with a polymer gate dielectric. For example, devices prepared by drop-casting or spin-coating TIPS-pentacene onto a CL-PVP gate dielectric showed hole mobilities of 2.08×10^{-2} and 3.95×10^{-3} cm^2/V·s[24,25], respectively. The charge carrier mobility was calculated from the saturation region of the transfer curves with the following Equation (1):

$$I_{DS} = \frac{W}{2L}\mu C_i(V_{GS} - V_{Th})^2$$

(1)

where C_i is the capacitance per unit area (61.04 pF/mm^2), I_{DS} is the drain-source current, μ is the field-effect mobility, V_{GS} is the gate voltage, V_{Th} is the threshold voltage, and L and W are the channel length and width, respectively. The subthreshold swing (*ss*), a measure of the switching speed of the device, is calculated by Equation (2):

$$ss = \left[\frac{d\log(I_{DS})}{dV_{GS}}\right]^{-1}$$

(2)

A top-contact *n*-channel uni-OFET based on a $F_{16}CuPc$ thin-film was also fabricated and characterized. The surface morphology of the $F_{16}CuPc$ film grown on the polymer gate dielectric at room temperature was investigated using AFM, as shown in the inset of Fig. 3(d). The results indicate that the film is consisted of numerous small grains; a similar morphology was also observed by others.[26] The output characteristics (I_{DS} vs. V_{DS}) at different V_{GS} show typical *n*-type behavior with dominant electron transport [supporting information (Fig. S2)]. The transfer (I_{DS} vs. V_{GS}) characteristic curves of the OFETs based on a $F_{16}CuPc$ thin film are depicted in Fig. 3(d). The device shows a moderate charge carrier mobility (μ_e) of 2.1×10^{-3} cm^2/V·s and a threshold voltage (V_{Th}) of 22.6 V,

which is comparable to previously reported devices fabricated using $F_{16}CuPc$ thin films, even though a CL-PVP gate dielectric was used in this study. Wang *et al.* reported an electron mobility of 7.6×10^{-3} $cm^2/V \cdot s$ in a $F_{16}CuPc$-based device fabricated by vacuum deposition onto a SiO_2/Si substrate.[27]

After characterizing the *p*- and *n*-type uni-OFETs, we fabricated ambi-OFETs with a microcrystal array-embedded active layer with the alternating *p*- and *n*- channel. A schematic of the formation of the ambi-OFETs is shown in Fig. 2. TIPS-pentacene microcrystal array embedded active layer was formed by depositing $F_{16}CuPc$ on and in between the crystals. The surface morphology of $F_{16}CuPc$ layer (deposited on and in between) is studied by AFM and discussed in supporting information (Fig. S3). The actual structure of the ambi-OFET with the microcrystal-embedded active layer was investigated using cross-sectional scanning electron microscopy (SEM) images. The device was cut vertically, and the micrographs were taken at different positions (Fig. 4). The cross-sectional SEM image [Fig. 4(a)] of the device shows that the layer consisted of *ca.* 32-nm-sized TIPS-pentacene and 135-nm-sized $F_{16}CuPc$. In Fig. 4(b), the image at the edge of the microwire shows the presence of both TIPS-pentacene with $F_{16}CuPc$ (left side of the image) and only $F_{16}CuPc$ (right side of the image) as active layer materials. These pictures confirm the formation of the microcrystal array-embedded active layer between the source and drain electrodes.

The output (I_{DS} vs. V_{DS}) and transfer (I_{DS} vs. V_{GS}) characteristics of the ambi-OFET based on the microcrystal-embedded thin-film layer are presented in Fig. 5(a) and 5(b), respectively. The curves clearly exhibit ambipolar current modulation. Typical output curves of an *n*-channel OFET are shown when high positive V_{DS} and V_{GS} were applied. On the other hand, at applied higher negative V_{DS} and V_{GS}, typical output curves of a *p*-channel OFET are observed. In the low V_{GS} region, an exponential increase in the drain current because of the opposite charge carrier is observed [shown in the second and fourth quadrants of Fig. 5(a)] with increasing V_{DS} on both sides (positive and negative V_{DS} and V_{GS}). The saturation region of the drain current at lower V_{GS} values is not observed in the output characteristics of the device. Application of higher positive and negative gate voltages suppressed this component, and typical saturation characteristics of *n*- and *p*-channel OFETs were observed. This type

of behavior has been previously reported in ambipolar OFETs.[27,28] These characteristics are because of the simultaneous existence of both types of charge carriers (electron and hole) in one device.

The relative difference in the gate and drain electrode voltages in the low V_{GS} regions results in the formation of the opposite charge carrier in the channel between the source and drain. Also, the presence of the heterojunction effect, as shown in Fig. 6 (right side), between TIPS-pentacene and $F_{16}CuPc$ results in the accumulation of holes and electrons in the TIPS-pentacene and $F_{16}CuPc$ layers, respectively. This transfer of charge carriers between TIPS-pentacene and $F_{16}CuPc$ is more clearly explained by the energy level diagram shown in Fig. 6 (right side). The energy levels of TIPS-pentacene and $F_{16}CuPc$ were obtained from previous reports,[29] with the highest occupied molecular orbital (HOMO) energy level of TIPS-pentacene at 5.16 eV, and the lowest unoccupied molecular orbital (LUMO) energy level of $F_{16}CuPc$ at 4.8 eV. The work function of the *n*-type semiconductor ($F_{16}CuPc$) is greater than that of the *p*-type semiconductor (TIPS-pentacene). Hence, the electron energy in TIPS-pentacene is smaller than the electron energy in $F_{16}CuPc$. Therefore, when TIPS-pentacene and $F_{16}CuPc$ come into contact, a heterojunction is formed between TIPS-pentacene and $F_{16}CuPc$. This results in electron transfer from TIPS-pentacene to $F_{16}CuPc$, and holes move into the TIPS-pentacene layer, leading to the accumulation of electrons in $F_{16}CuPc$ and holes in TIPS-pentacene (Fig. 6, right side). These accumulated electrons and holes at the interface also contribute to the current because of the opposite charge carriers in the lower $\pm V_{GS}$ regions. Various groups have observed similar phenomena in organic/organic ($CuPc/F_{16}CuPc$, $ZnPc/F_{16}ZnPc$, $BP_2T/F_{16}CuPc$, and pentacene/$F_{16}CuPc$) heterojunctions.[27,28,30] The above explanations clarify the ambipolar behavior observed in the output characteristic curves of the device.

On the other hand, at applied higher negative voltage, holes were induced at the interface between the TIPS-pentacene 1D-microwires and CL-PVP, as shown in Fig. 6. Hole channels were formed using the TIPS-pentacene 1D-microwires, and the drain current increased with increasing V_{DS} at a constant V_{GS}. Similarly, at high positive V_{GS} values, electrons accumulated at the $F_{16}CuPc/CL-PVP$ interface, and an electron channel formed in the $F_{16}CuPc$ layer, as shown in Fig. 6. In the bilayered

ambipolar OFETs reported in the literature (discussed above), only one type of semiconductor is in direct contact with the gate dielectric. Hence, in bilayered ambipolar OFETs such as $F_{16}CuPc/CuPc$, electron and hole channels are formed at the $F_{16}CuPc/CuPc$ and $CuPc/SiO_2$ interfaces, respectively. In our device structure, both TIPS-pentacene and $F_{16}CuPc$ are in direct contact with the polymer gate dielectric, and alternating *p*- and *n*-channels are formed, as shown in Fig. 6.

Fig. 5(b) shows the transfer characteristics of the ambi-OFETs for both positive and negative gate biases in the saturation regime ($V_{DS} = \pm60$ V). The value of the drain current originates from the hole charges increasing continuously for $V_{DS} = -60$ V (when $V_{GS} < -28$ V). On the other hand, when the applied $V_{GS} > -28$ V, the increasing drain current may be responsible for the electron transport. The field-effect mobility for the hole current is found to be 3.4×10^{-3} cm^2/V·s. The electron current also shows similar electrical behavior. For $V_{DS} = 60$ V, the electron-enhancement mode is observed at applied $V_{GS} > 17$ V. The value of the drain current, originating from the electron charges, increases continuously for $V_{DS} = 60$ V (when $V_{GS} > 17$ V). Similarly, when the applied $V_{GS} < 17$ V, the increasing drain current may be responsible for the hole transport. The field-effect mobility for the electron current is estimated to be 1.4×10^{-4} cm^2/V·s. The performance parameters of unipolar and ambipolar OFETs are also summarized in Table 1. These devices are very stable in air (note that all measurements were performed in ambient conditions without encapsulation).

In order to demonstrate the potential of our ambi-OFET device for applications in organic microelectronics, we fabricated complementary-like inverters employing two identical ambi-OFETs and analyzed their performance. The upper left panel of Fig. 7 shows a schematic diagram of the complementary-like inverter structure. We observe symmetric output curves with significant signal gain (typically in the range 6-8). Both the OFETs used in this study shows good ambipolar output characteristics with applied respective positive and negative gate and drain voltages. The output characteristics of both the ambi-OFETs are presented in supporting information (Fig. S4). The complementary-like inverters show the unique characteristic of operating both in the first and third quadrants of the V_{OUT} versus V_{IN} plot without changing the circuitry.[13] Our complementary-like

voltage inverter, fabricated using identical ambipolar OFETs, shows voltage transfer characteristics (V_{TC}) in both quadrants (first and third) with applied V_{DD} and V_{IN}. With an applied positive supply voltage (V_{DD}) and positive V_{IN}, the inverter works in the first quadrant (Fig. 7). Under the above bias conditions, OFET 1 acts mainly like a *p*-type transistor of a regular CMOS-like inverter, while OFET 2 operates as the *n*-type transistor. On the other hand, when the applied input voltage and V_{DD} are negative, the inverter still operates with an *n*-channel (OFET 1) and a *p*-channel (OFET 2), switching the performance to the third quadrant. The voltage gain (defined as the absolute value of (dV_{OUT}/dV_{IN}), output voltage swing (defined as V^{max}_{OUT} - V^{min}_{OUT}), and noise margin are calculated from the voltage transfer curves. When a supply voltage (V_{DD}) of 60 V was biased to the inverter, the output voltage (V_{OUT}) varies from high to low in response to the swing of the input voltage (V_{IN}) from low to high, and a sharp inversion of V_{IN} is found near 36.3 and 41.5 V in the forward and reverse cycles, respectively. The maximum voltage gain reaches a value of 7.6 and 6.1 in the forward and reverse scans, respectively (see the lower-right part of Fig. 7). Similar characteristics are observed when a supply voltage of -60 V is applied. Inversion in the device characteristics is seen at -31.4 and -26.0 V in the forward and reverse scans with gain values of 8.0 and 7.4, respectively. From these V_{TC} values, we calculated the voltage input low (V_{IL}), voltage input high (V_{IH}), voltage output low (V_{OL}), and voltage output high (V_{OH}) for the forward and reverse biases by applying V_{DD} = ±60 V. The relative values of low and high noise margins are calculated by the formulas $NM_H = V_{OH}$ - V_{IH} and $NM_L = V_{IL}$ - V_{OL}. With a positive V_{DD} of 60 V, the values of the noise margin at low and high voltages are 13.8, 13.5 and 12.4, 8.2 V in the forward and reverse biases, respectively. Similarly, these values are -19.0, -18.7 and -15.2, -20.1 V in the forward and reverse biases, respectively, when a V_{DD} of -60 V is applied. Table 2 summarizes the gain values and noise margin results of the complementary-like voltage inverter. Finally, load type inverter based on ambi-OFET having alternating *p*- and *n*-channel have been constructed and analyzed. The output and transfer characteristic of the ambi-OFET is depicted in supporting information (Fig. S5). Fig. 8 shows that the typical transient response of ambi-OFET based inverter at constant V_{DD}, when the V_{IN} is pulsed at 10 Hz. Fig. 8 (a) depicts the circuit diagram of the

load inverter. Fig. 8 (b) and 8 (c) demonstrate decent inversion characteristics with a load resistor of 20 MΩ, while V_{DD} was kept at -60 V and +60 V, respectively. As shown in V_{OUT}, the studied device clearly shows both PMOS-like and NMOS-like load type organic inverter characteristics when V_{IN} was swept between 0 to -60 V and 0 to +60 V, respectively. Frequency dependent PMOS-like and NMOS-like load type organic inverter characteristics have also been recorded and depicted in supporting information (Fig. S6 and Fig. S7). Hence, our unique ambi-OFET device structure based inverter shows well behaved static as well as dynamic characteristics. The rising (t_r) and falling (t_f) times of V_{OUT} are obtained as 26.9 and 10.3 ms, respectively for PMOS and, 15.2 and 14.6 ms, respectively for NMOS-like load type organic inverter.

Conclusion

In summary, we successfully fabricated air-stable ambipolar organic thin-film transistors and inverters based on solution-processed TIPS-pentacene 1D-microwires and a $F_{16}CuPc$ thin film. We report unique device architecture in which $F_{16}CuPc$ was deposited on and between the ordered crystalline microwires of TIPS-pentacene, resulting in the formation of direct alternating *n*- and *p*-channels between the source and drain. The present device shows high ambipolarity (> 90%) with charge transport values of 3.4×10^{-3} cm^2/V·s for hole and 1.4×10^{-4} cm^2/V·s for electron. The complementary-like inverter based on two identical ambipolar transistors exhibits a high gain of ~8. Further improvement may be achieved by changing the thickness of the $F_{16}CuPc$ layer or by using other organic materials with higher mobilities.

Experimental section

OFETs with bottom-gate and top-contact geometry are used in the present study. All the materials, including TIPS-pentacene, $F_{16}CuPc$, poly(4-vinylphenol), poly(melamine-*co*-formaldehyde), and propylene glycol monomethyl ether acetate were purchased from Aldrich Chemical Co., and the materials were used as supplied. All devices were fabricated on a photo-lithographically patterned

indium-tin oxide (ITO)-coated glass substrate, which was precleaned using detergent, deionized water, acetone, and isopropyl alcohol in an ultrasonic bath and dried in a drying oven. Thermally cross-linkable polymer, prepared by mixing poly(4-vinylphenol) and poly(melamine-*co*-formaldehyde), was used as a gate dielectric. Before the deposition of the gate dielectric, the ITO substrate was cleaned with UV-ozone cleaner for 80 s. The prepared dielectric precursor solution was spin-coated on the substrate and soft-baked for 3 min on a hot plate (90 °C) and baked further in a vacuum oven (10^{-3} Torr) at 175 °C for 1 h. The thickness of the gate dielectric layer was 480 nm as measured by Alpha-step (XP-100). In the Uni-OFET devices, the TIPS-pentacene microcrystal array (Fig. 1a) and $F_{16}CuPc$ (Fig. 1b) were directly deposited on the gate dielectric as the active layer. Kai and Karthaus *et. al*, have also reported crystal formation method by using a moving glass roller fitted with a concentric spacer at constant speed to form a thin liquid stripe on the substrate and the volatile solvent is allowed to evaporate along the straight three-phase-line, that is the contact line of the liquid with the substrate.[31] The TIPS-pentacene crystal array was grown by dropping a solution of TIPS-pentacene in *o*-dichlorobenzene (0.1 wt%) over the capillary tube placed along the direction of the patterned ITO gate electrode, followed by drying of the dropped solution on a hot plate (90 °C) for 1 h under ambient conditions. After complete evaporation of the solvent, crystals had grown on both sides of the tube in directions normal to its length. This orientation of so formed crystals arise from capillary forces between the tube and the organic semiconductor solution. In addition, more compact and alined ordered nano/micro crystal rods arrises due to induced force from continuous shrinkage of the solid/liquid interfacial area during evaporation. A detailed procedure and mechanism was described in our previous communication.[23(a)] The $F_{16}CuPc$ (140 nm) film was vacuum-deposited by thermal evaporation at a rate of 0.1 Å/s with the substrate temperature fixed at 25 °C. In the Ambi-OFET device [Fig. 1(c)], the organic microcrystal array-embedded active layer with highly directional alternating *n*- and *p*-channels was prepared by successive deposition of $F_{16}CuPc$ on top of the microcrystal. For the completion of the top-contact Uni- and Ambi-OFETs, gold (Au) (50 nm) was thermally evaporated under a high vacuum (5×10^{-6} Torr) at a rate of 0.3 Å/s as a source-drain

electrode. The procedure is depicted in Fig. 2. The dimensions, channel length (*L*), and width (*W*) of the device were defined by the metal shadow mask used for the gold electrode deposition, but the actual values varied according to the device structure. For the Uni-OFET devices with TIPS-pentacene microwires, the channel length (*L*) was 50 μm, and the width (*W*) was calculated as the sum of the width of the microcrystals lying in the channel as measured by polarized optical microscopy (Olympus BX 51). For the Uni-OFET devices with a $F_{16}CuPc$ thin film, *L* and *W* were 50 and 1000 μm, respectively. *L* and *W* of the Ambi-OFET were calculated in the same manner as the Uni-OFETs. In the complementary inverters comprised of two Ambi-OFETs, the channel width was changed to 4000 μm in order to match the hole and electron current level. Atomic force microscopy (AFM) and scanning electron microscopy measurements of the deposited films were performed with nanoscope IIIa (Veeco, digital instruments) and an SEM (TESCAN FESEM MIRA II), respectively. Electrical characterization of the devices was carried out under ambient conditions using an HP semiconductor parameter analyzer (HP 4145B).

Acknowledgements

Notes and references

1. (a) J. Kawahara, P. A. Ersman, D. Nilsson, K. Katoh, Y. Nakata, M. Sandberg, M. Nilsson, G. Gustafsson and M. Berggren, *J. Polym. Sci. B: Polym. Phy.,* 2013, **51**, 265; (b) J. H. Park, T. W. Koh, J. Chung, S. H. Park, M. Eo, Y. Do, S. Yoo and M. H. Lee, *Macromolecules,* 2013, **46**, 674; (c) S. Basak, Y. S. L. V. Narayana, M. Baumgarten, K. Mullen and R. Chandrasekar, *Macromolecules*, 2013, **46**, 362.

2. (a) A. K. Palai, J. Lee, S. Das, J. Lee, H. Cho, S. -U. Park and S. Pyo, *Org. Electron.,* 2012, **13**, 2553.; (b) S. Das, J. Lee, T. Lim, Y. Choi, Y. S. Park and S. Pyo, *Synth. Met.,* 2012, **162**, 598; (c)

Q. Wu, R. Li, W. Hong, H. Li, X. Gao and D. Zhu, *Chem. Mater.,* 2011, **23**, 3138; (d) B. Lucas, T. Trigaud and C. V. Ackermann, *Polym. Int.,* 2012, **61**, 374.

3. (a) J. Sun, Y. Zhu, X. Xu, L. Lan, L. Zhang, P. Cai, J. Chen, J. Peng and Y. Cao, *J. Phys. Chem. C,* 2012, **116**, 14188; (b) Y. J. Hwang, G. Ren, N. M. Murari and S. A. Jenekhe, *Macromolecules,* 2012, **45**, 9056.

4. C. Ruiz, E. M. García-Frutos, G. Hennrich and B. Gomez-Lor, *J. Phys. Chem. Lett.,* 2012, **3**, 1428.

5. (a) J. Zhang, C. Wang and C. Zhou, *ACS nano,* 2012, **6**, 7412; (b) P. Lin and F. Yan, *Adv. Mater.,* 2012, **24**, 34; (c) G. Gelinck, P. Heremans, K. Nomoto and T. D. Anthopoulos, *Adv. Mater.,* 2010, **22**, 3778.

6. (a) A. K. Palai, H. Cho, S. Cho, T. J. Shin, S. Jang, S. -U. Park and S. Pyo, *Org. Electron.,* 2013, **14**, 1396; (b) J. Smith, M. Heeney, I. McCulloch, J. N. Malik, N. Stingelin, D. D. C. Bradley and T. D. Anthopoulos, *Org. Electron.,* 2011, **12**, 143; (c) C. Mitsui, J. Soeda, K. Miwa, H. Tsuji, J. Takeya and E. Nakamura, *J. Am. Chem. Soc.,* 2012, **134**, 5448; (d) K. J. Baeg, D. Khim, S. W. Jung, M. Kang, I. K. You, D. Y. Kim, A. Facchetti and Y. Y. Noh, *Adv. Mater.,* 2012, **24**, 5433.

7. (a) M. Mukherjee, B. Mukherjee, Y. Choi, K. Sim, J. Do and S. Pyo, *Synth. Met.,* 2010, **160**, 504; (b) H. Zhong, J. Smith , S. Rossbauer, A. J. P. White, T. D. Anthopoulos and M. Heeney, *Adv. Mater.,* 2012, **24**, 3205; (c) S. G. Hahm, Y. Rho, J. Jung, S. H. Kim, T. Sajoto, F. S. Kim, S. Barlow, C. E. Park, S. A. Jenekhe, S. R. Marder and M. Ree, *Adv. Funct. Mater.,* 2013, **23**, 2060; (d) J. -E. Park, B. Mukherjee, H. Cho, S. Kim and S. Pyo, *Synth. Met.,* 2011, **161**, 143.

8. A. Opitz, M. Horlet, M. Kiwull, J. Wagner, M. Kraus and W. Brutting, *Org. Electron.,* 2012, **13**, 1614.

9. (a) R. Capelli, S. Toffanin, G. Generali, H. Usta, A. Facchetti and M. Muccini, *Nat. Mater.,* 2010, **9**, 496; (b) K. Sawabe, M. Imakawa, M. Nakano, T. Yamao, S. Hotta, Y. Iwasa and T. Takenobu, *Adv. Mater.,* 2012, **24**, 6141; (c) M. A. McCarthy, B. Liu, E. P. Donoghue, I. Kravchenko, D. Y. Kim, F. So and A. G. Rinzler, *Science,* 2011, **332**, 570.

10. (a) J. D. Oh, H. S. Seo, D. K. Kim, E. S. Shin and J. H. Choi, *Org. Electron.,* 2012, **13**, 2192; (b) J. C. Ribierre, T. Fujihara, T. Muto and T. Aoyama, *Org. Electron.,* 2010, **11**, 1469.

11. B. Crone, A. Dodabalapur, Y. Y. Lin, R. W. Filas, Z. Bao, A. LaDuca, R. Sarpeshkar, H. E. Katz and W. Li, *Nature,* 2000, **403**, 521.

12. (a) P. Sonar, T. R. B. Foong, S. P. Singh, Y. Li and A. Dodabalapur, *Chem. Commun.,* 2012, **48**, 8383; (b) W. Hong, B. Sun, H. Aziz, W. T. Park, Y. Y. Noh and L. Yuning, *Chem. Commun.,* 2012, **48**, 8413; (c) T. Sugawara, T. Itoh, K. Suzuki, H. Higuchi and M. M. Matsushita, *Pure Appl. Chem.,* 2012, **84**, 979; (d) J. Kan, Y.Chen, D. Qi, Y. Liu and J. Jiang, *Adv. Mater.,* 2012, **24**, 1755.

13. E. J. Meijer, D. M. deLeeuw, S. Setayesh, V. E. Van, B. H. Huisman, P. W. Blom, J. C. Hummelen, U. Scherf, J. Kadam and T. M. Klapwijk, *Nat. Mater.,* 2003, **2**, 678.

14. (a) M. Treier, J. B. Arlin, C. Ruzi, Y. H. Geerts, V. Lemaur, J. Cornil and P. Samor, *J. Mater. Chem.,* 2012, **22**, 9509; (b) Y. Hu, N. Zhang, J. Lin, L. Qin and X. Liu, *Appl. Phys. Express,* 2012, **5**, 095601.

15. A. Dodabalapur, H. E. Katz, L. Torsi and R. C. Haddon, *Science,* 1995, **269**, 1560.

16. S. D. Wang, K. Kanai, Y. Ouchi and K. Seki, *Org. Electron.,* 2006, **7**, 457.

17. J. Wang, H. Wang, X. Yan, H. Huang and D. Yan, *Chem. Phys. Lett.,* 2005, **407**, 87.

18. B. J. Shi, H. Wang, D. Song, H. Tian, Y. Geng and D. Yan, *Adv. Funct. Mater.,* 2007, **17**, 397.

19. K. N. N. Unni, A. K. Pandey, S. Alem and J. M. Nunzi, *Chem. Phys. Lett.,* 2006, **421**, 554.

20. C. Yang, Y. Kwack, S. H. Kim, T. K. An, K. Hong, S. Nama, M. Park, W. S. Choi and C. E. Park, *Org. Electron.,* 2011, **12**, 411.

21. (a) S. Kim, T. Lim, K. Sim, H. Kim, Y. Choi, K. Park and S. Pyo, *ACS Appl. Mater. Interfaces,* 2011, **3**, 1451; (b) C. Keil and D. Schlettwein, *Org. Electron.* 2011, **12**, 1376; (c) S, C. Martens, U, Zschieschang, H. Wadepohl, H. Klaukm and L. H. Gade, *Chem. Eur. J.,* 2012, **18**, 3498.

22. (a) D. H. Kim, D. Y. Lee, S. G. Lee and K. Cho, *Chem. Mater.*, 2012, **24**, 2752; (b) H. S. Seo, J. D. Oh, D. K. Kim, E. S. Shin and J. H. Choi, *J. Phys. D: Appl. Phys.,* 2012, **45**, 505108.

23. (a) B. Mukherjee, T. J. Shin, K. Sim, M. Mukherjee, J. Lee, S. Kim and S. Pyo, *J. Mater. Chem.*, **2010**, *20*, 9047; (b) B. Mukherjee, M. Mukherjee, K. Sim and S. Pyo, *J. Mater. Chem.,* 2011, **21**, 1931; (c) B. Mukherjee, K. Sim, T. J. Shin, J. Lee, M. Mukherjee, M. Ree and S. Pyo, *J. Mater. Chem.,* 2012, **22**, 3192; (d) A. K. Palai, J. Lee, S. Das, J. Lee, H. Cho, S. U. Park and S. Pyo, *Org. Electron.,* 2012, **13**, 2553.

24. S. I. Shin, J. H. Kwon, H. Kang and B. K. Ju, *Semicond. Sci. Technol.,* 2008, **23**, 085009.

25. P. Tassini, M. G. Maglione, R. Rega, A. D. G. D. Mauro, T. Fasolino, G. Pandolfi, E. Calo, C. Minarini and P. Maddalena, *AIP Conf. Proc.,* 2012, **1459**, 262.

26. Z. Bao, A. J. Lovinger and J. Brown, *J. Am. Chem. Soc.,* 1998, **120**, 207.

27. (a) J. Zaumseil and H. Sirringhaus, *Chem. Rev.* 2007, **107**, 1296; (b) J. Wang, H. Wang, X. Yan, H. Huang, D. Jin, J. Shi, Y. Tang and D. Yan, *Adv. Funct. Mater.,* 2006, **16**, 824.

28. F. Hong, F. Xing, W. Gu, W. Jin, J. Zhang and J. Wang, *Synth. Met.,* 2010, **160**, 475.

29. (a) Y.-F. Lim, Y. Shu, S. R. Parkin, J. E. Anthony and G. G. Malliaras, *J. Mater. Chem.,* 2009, **19**, 3049; (b) H. Peisert, M. Knupfer, T. Schwieger, G. G. Fuentes, D. Olligs, J. Fink and Th. Schmidt, *J. Appl. Phys.,* 2003, **3**, 9683.

30. D. Schlettwein, K. Hesse, N. E. Gruhn, P. A. Lee, K. W. Nebesny and N. R. Armstrong, *J. Phys. Chem. B,* 2001, **105**, 4791.

31. (a) O. Karthaus, S. Nagata, Y. Kiyono, S. Ito, H. Miyasaka, *Colloids and Surfaces A: Physicochem. Eng. Aspects,* 2008, **313-314**, 571; (b) K. Kai, O. Karthaus, *e-Journal of Surface Science and Nanotechnology*, 2007, **5**,103.

Footnote
Electronic supporting information (ESI) is available online from the The Royal Society of Chemistry or from the author.
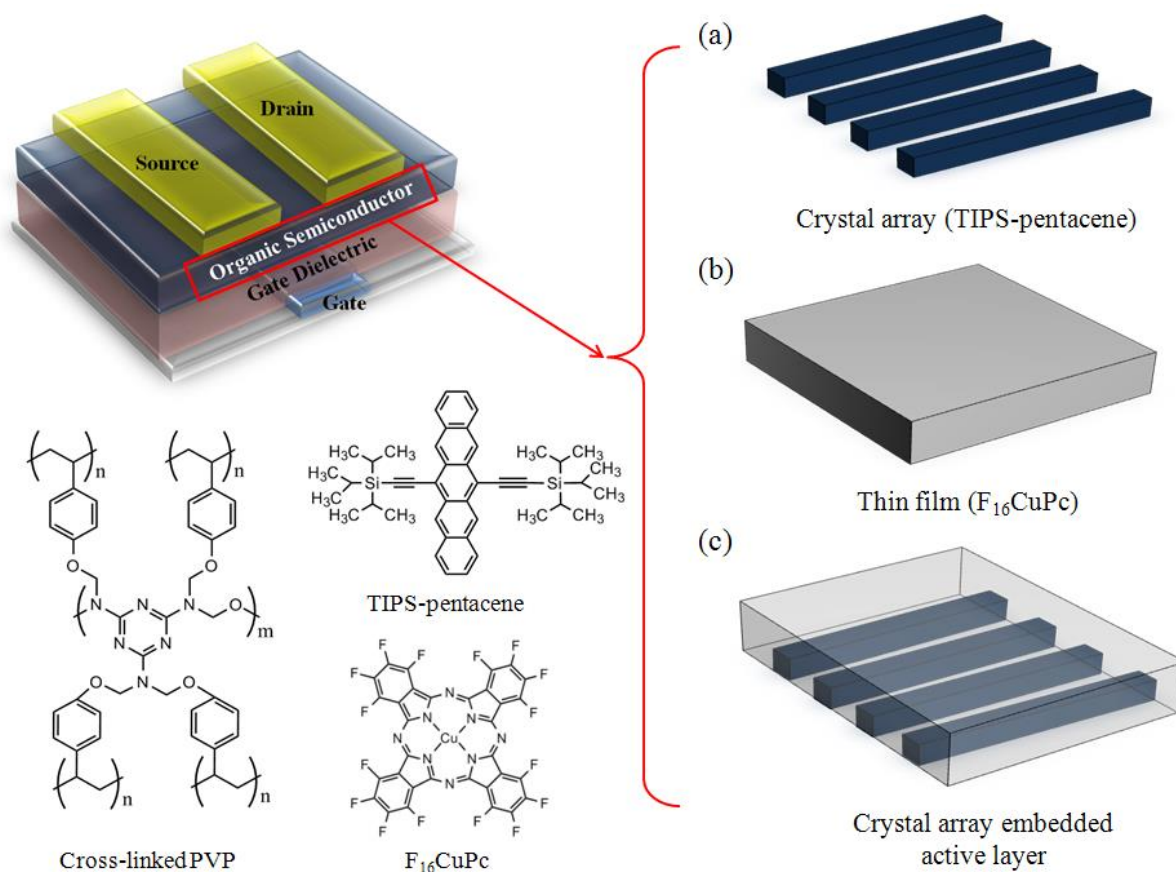
Fig. 1 Schematic of unipolar organic field-effect transistors (Uni-OFETs) based on (a) TIPS-pentacene microcrystal array, (b) $F_{16}CuPc$ thin film, and (c) ambipolar organic field-effect transistors (Ambi-OFETs). Chemical structure of TIPS-pentacene, $F_{16}CuPc$, and cross-linked poly(4-vinlyphenol) dielectric are also shown.
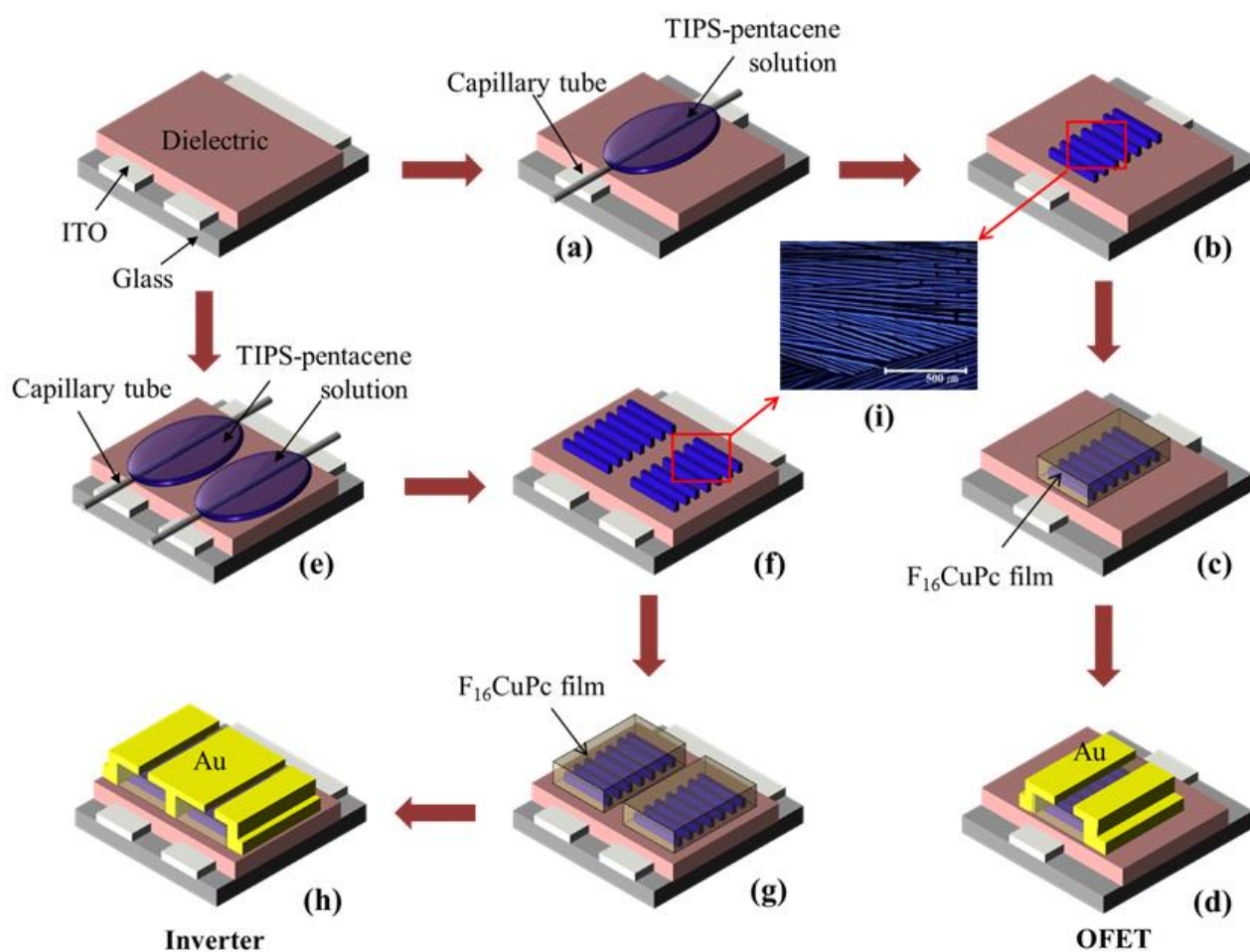
Fig. 2 Schematic of device fabrication: OFET [(a)–(d)] and inverter [(e)–(h)]. (a), (e) Capillary tube is

placed on top of dielectric film with its length parallel to patterned ITO gate electrode, and TIPS-

pentacene solution is dropped onto tube. (b), (f) Substrate is placed on hot plate and baked under

ambient conditions at 90 ℃ for 1 h. (c), (g) $F_{16}CuPc$ is deposited onto crystals for second organic

semiconductor. (d), (h) Au is deposited onto thin film to form top-contact source-drain electrodes for

OFET device. (i) The OM image of 1D-microwires of TIPS-pentacene, scale bar: 500 μm.

17
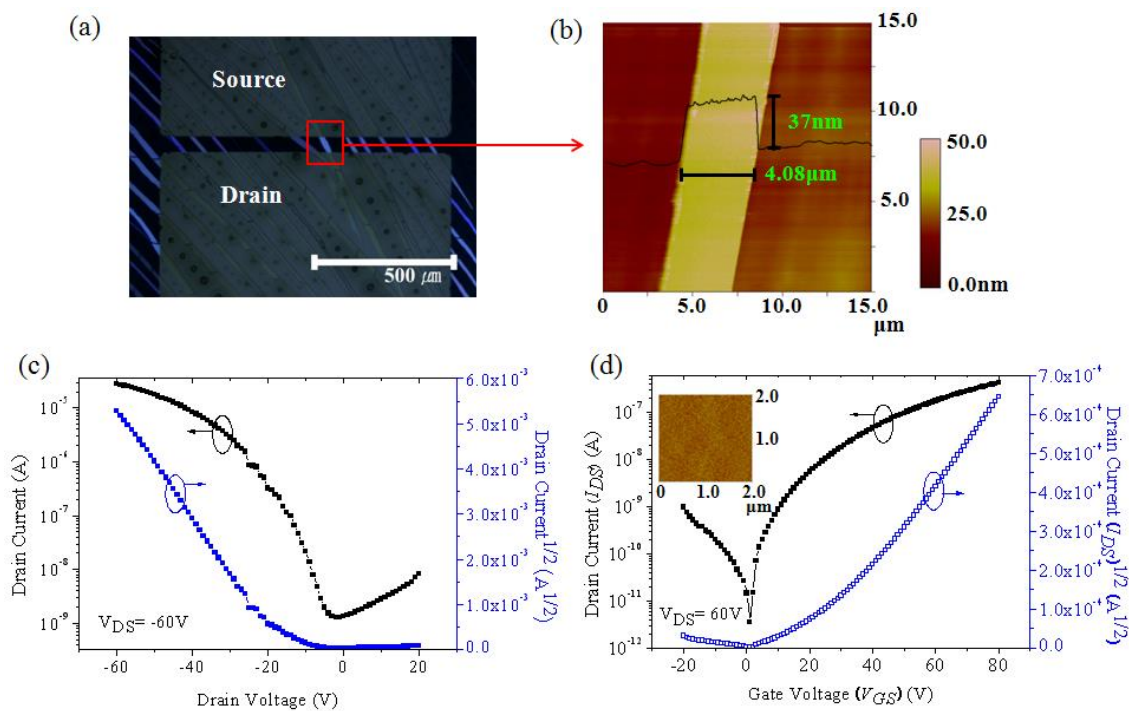
Fig. 3 (a) Representative polarized optical microscope image of 1D-microwires crossing source-drain electrodes. (b) AFM image of wires. (c) Transfer characteristic curves (V_{DS} = -60 V) of OFETs based on wires (*L* and *W* were 50 and 64 μm, respectively). (d) Transfer characteristic curves (V_{DS} = 60 V) of OFETs based on F_{16}CuPc thin film (*L* and *W* were 50 and 1000 μm, respectively). Inset shows AFM image (2 × 2 μm^2) of 100-nm-thick F_{16}CuPc film.
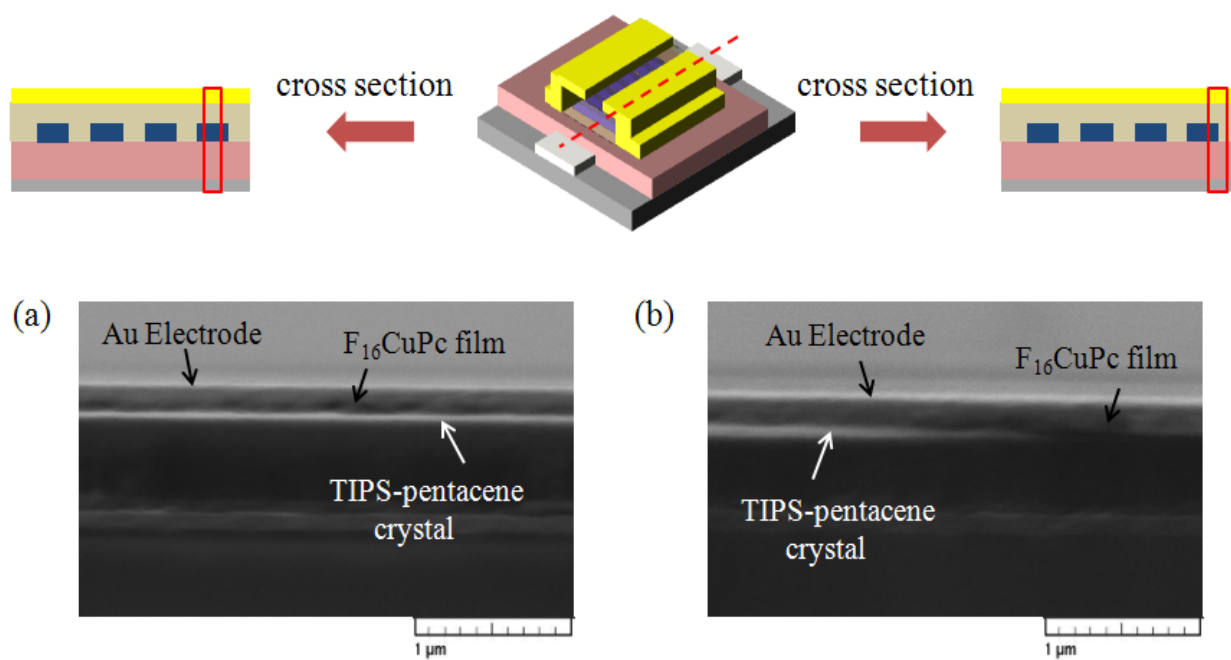
Fig. 4 (a) and (b) Cross-sectional SEM images of the ambi-OFET device based on micro-crystal embedded active layer at different cross section points
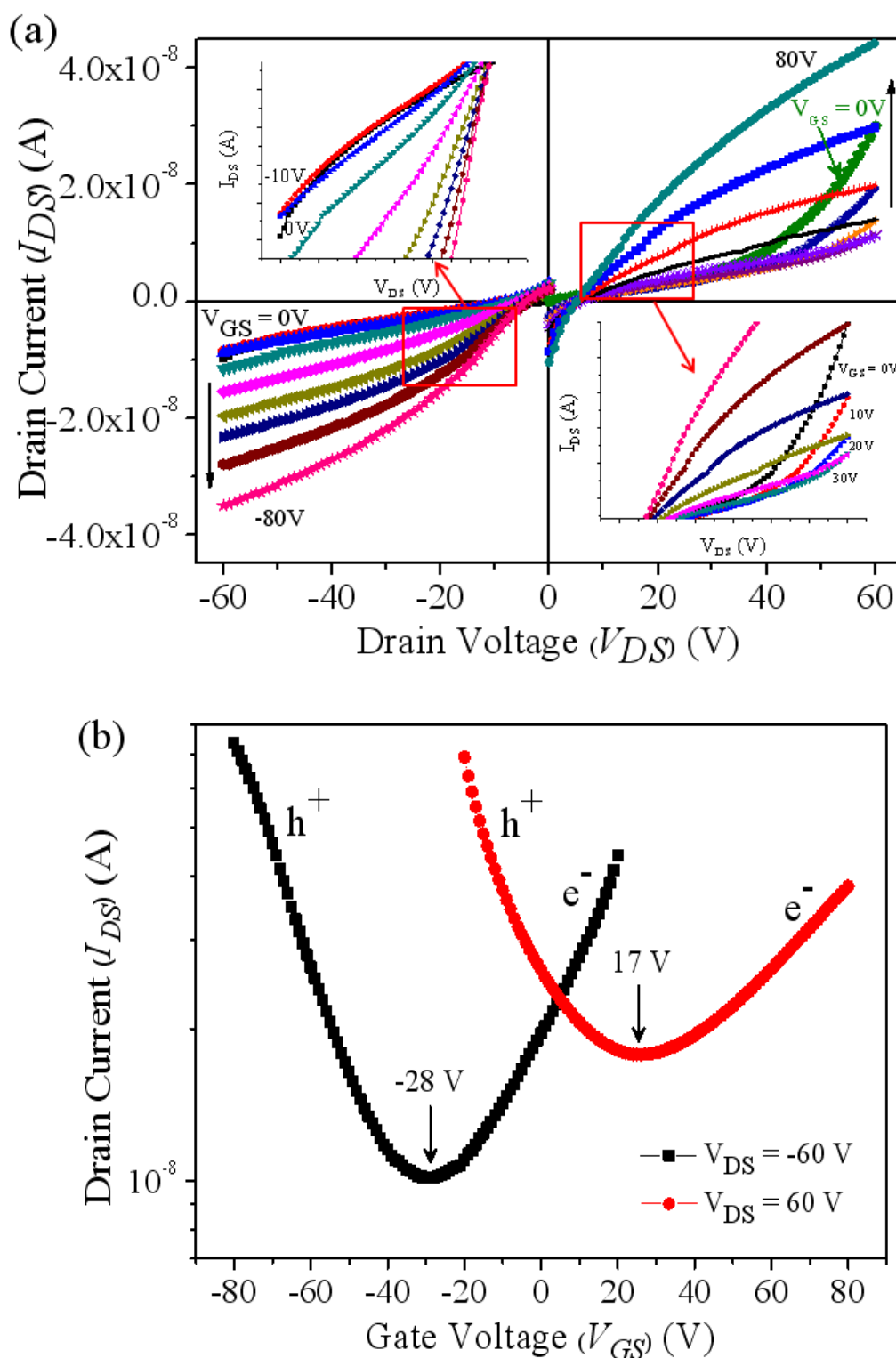
Fig. 5 (a) Output and (b) transfer (V_{DS} = 60 V and -60 V) characteristic curves of ambi-OFET based on TIPS-pentacene 1D-microwires and $F_{16}CuPc$ thin film. Inset (second and fourth quadrants): enlarged output of ambi-OFET at 0 and in low $|V_{GS}|$ region. (ambi-OFET, ambipolar organic field-effect transistor.
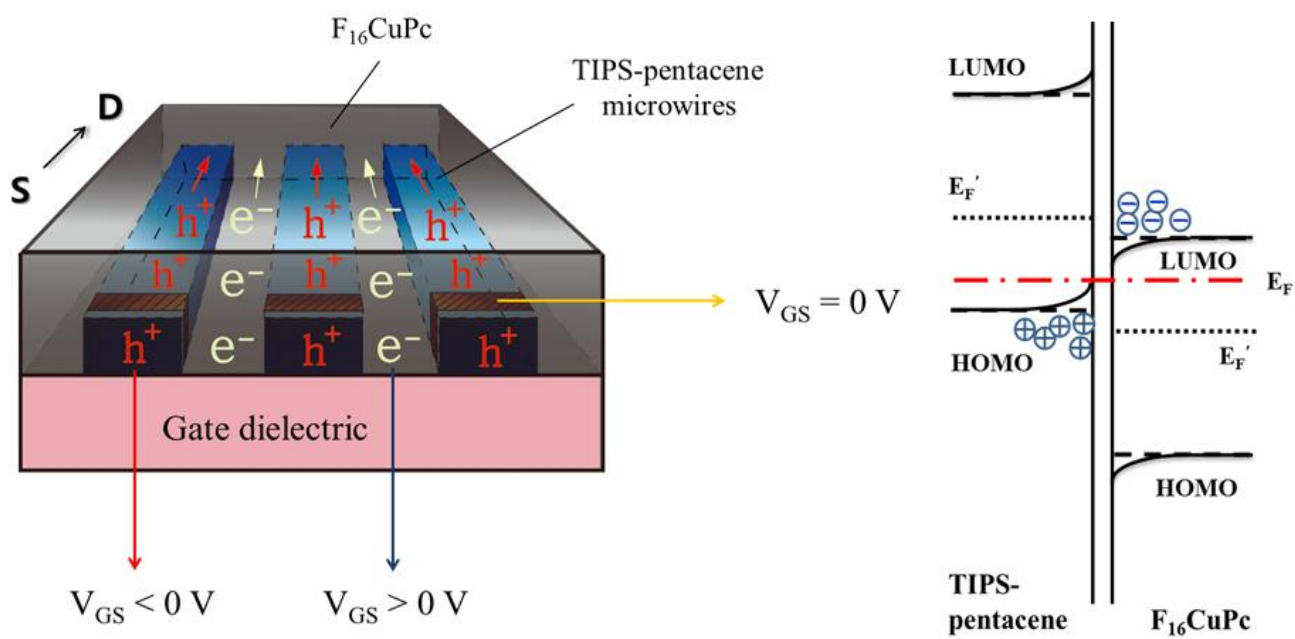
Fig. 6 Left side: conduction through different channels with respect to applied voltage. Right side: energy levels of TIPS-pentacene and F_{16}CuPc before (dotted lines) and after (solid line) contact. $E_{F'}$ and E_F represent Fermi levels before and after contact, respectively.
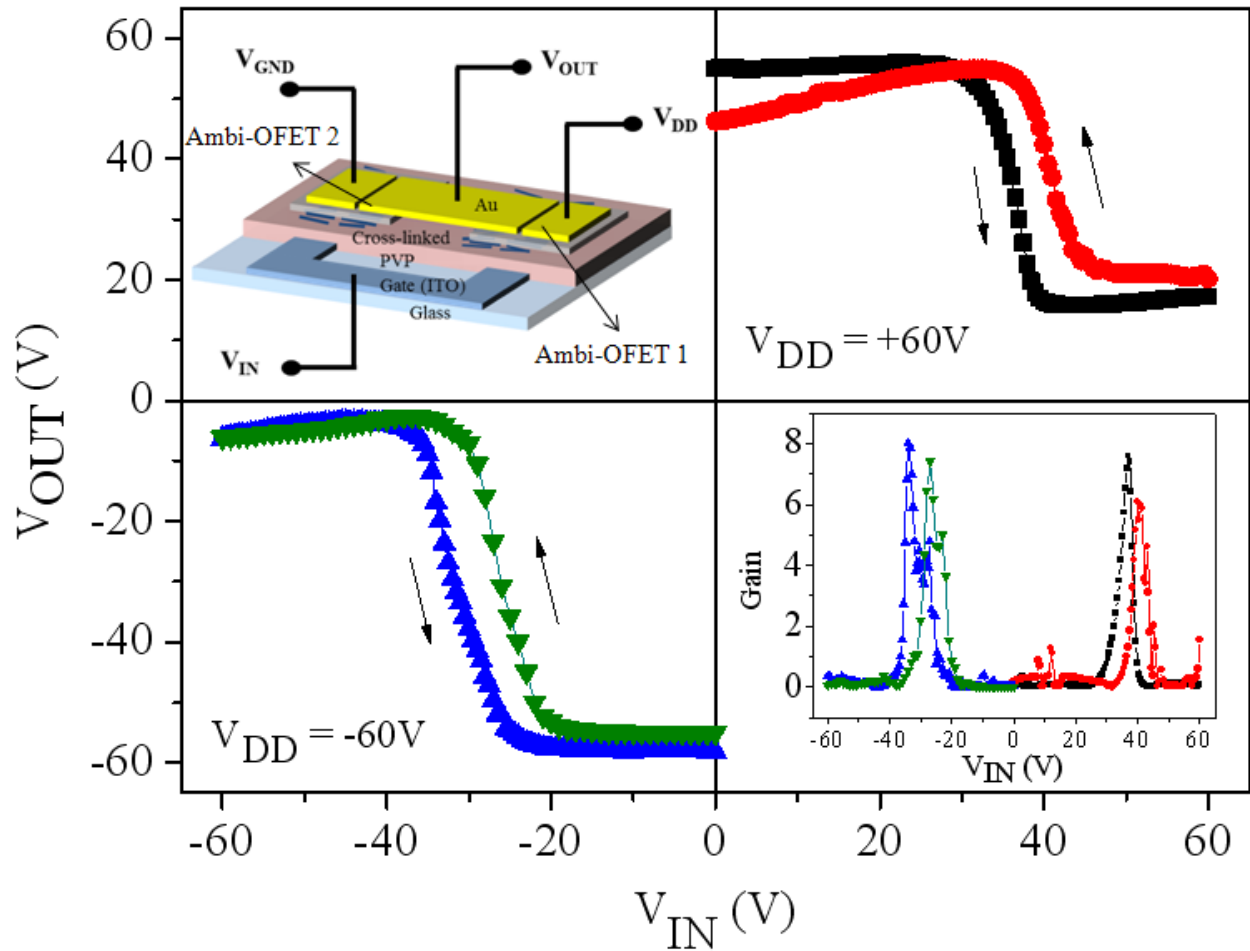
Fig. 7 Voltage transfer characteristics of complementary inverter with two identical ambipolar OFETs based on TIPS-pentacene 1D-microwires and $F_{16}CuPc$ film, drive voltage $V_{DD} = \pm 60$ V. Circuit diagram (upper-left) and gain (lower-right) of inverter are shown in inset.
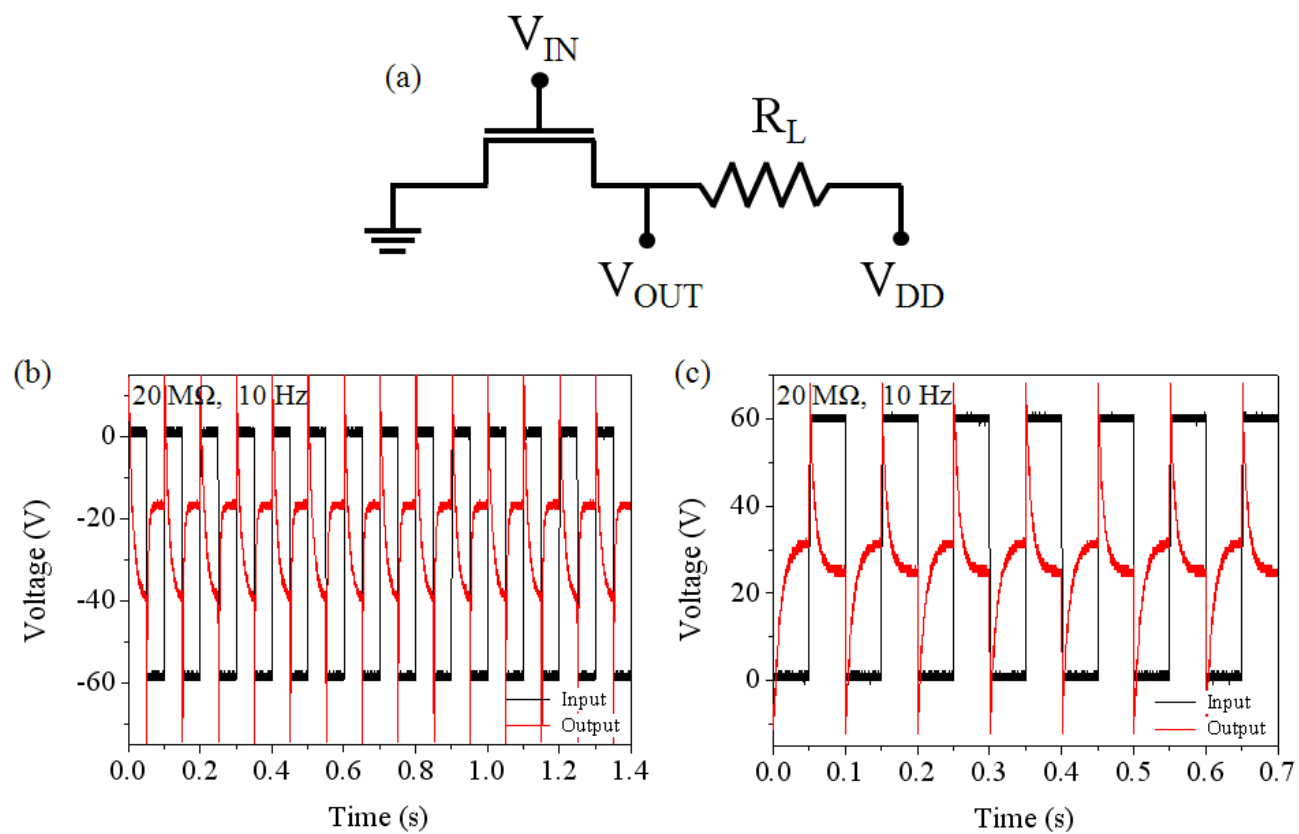
Fig. 8 The circuit diagram of the load inverter (a). The transient response of PMOS (b) and NMOS (c)

with a resistive load of 20 MΩ at constant drain bias when the gate voltage is pulsed at 10 Hz.

Table 1. Summary of performance parameters of uni-OFETs and ambi-OFETs.

		Mobility $(cm^2/V \cdot s)^a$	V_{Th} $(V)^b$	SS $(V\ decade^{-1})^c$	$I_{On}/I_{Off}{}^d$
Uni-OFET	p-type (TIPS-pentacene)	7.2×10^{-1}	-15.7	5.6	2.2×10^4
	n-type ($F_{16}CuPc$)	2.1×10^{-3}	22.6	2.9	1.2×10^5
Ambi-OFET	p-type	3.4×10^{-3}	-28.3	-	7.0×10^0
	n-type	1.4×10^{-4}	16.9	37.7	3.9×10^0

[a]Charge carrier mobility, [b]Threshold voltage, [c]Subthreshold swing, [d]I_{ON}/I_{OFF} ratio
(uni-OFET, unipolar organic field-effect transistor; ambi-OFET, ambipolar organic field-effect transistor)

Table 2 Summary of performance of complementary-like inverter using two ambipolar organic field-effect transistors.

	V_M $(V)^a$	Gain	$NM_H{}^b$	$NM_L{}^c$
$V_{DD} = +60V$ forward	36.3	7.6	13.5	13.8
$V_{DD} = +60V$ reverse	41.5	6.1	8.2	12.4
$V_{DD} = -60V$ forward	-31.4	8.0	-18.7	-19.0
$V_{DD} = -60V$ reverse	-26.0	7.4	-21.0	-15.2

[a]Logic threshold. [b]Noise Margin High. [c]Noise Margin Low

Supporting Information

Organic Microcrystal Array-Embedded Layer: Highly Directional Alternating *p*- and *n*-Channel for Ambipolar Transistor and Inverter

Minkyung Jea, Amit Kumar, Hyejin Cho, Dongmyung Yang, Hyunseok Shim, Akshaya K. Palai,

Seungmoon Pyo*

Department of Chemistry, Konkuk University, 120 Neungdong-ro, Gwangjin-gu, Seoul 143-701,

Republic of Korea

Corresponding author: pyosm@konkuk.ac.kr
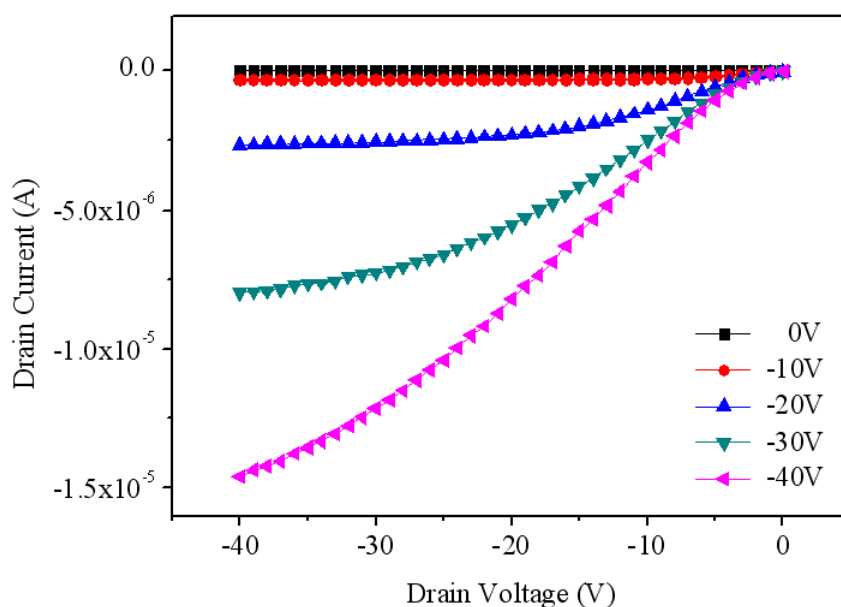
Fig. S1 Output (V_{GS} = 0 V ~ -40 V) characteristic curves of OFETs based on TIPS-pentacene 1D-microwires and 480 nm thick polymer gate dielectric. The channel length (*L*) and width (*W*) of the OFET were 50 and 64 μm, respectively.
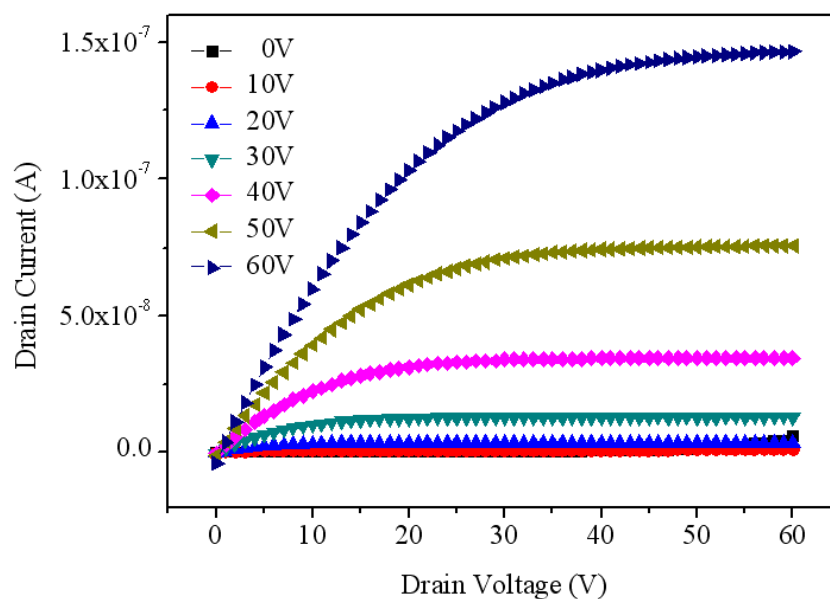
Fig. S2 Output (V_{GS} = 0 V ~ 60 V) characteristic curves of OFETs based on a single layer of F_{16}CuPc

(50 nm) thin-film grown by thermal evaporation on CL-PVP gate dielectric at room temperature. The

channel length (*L*) and width (*W*) of the OFETs were 50 and 1000 μm, respectively.

Morphological characteristics of F_{16}CuPc film deposited on and in between the TIPS-pentacene

microwires.

AFM images of the F_{16}CuPc film deposited on and in between 1D-microwires of TIPS-pentacene are

shown in Fig. S3. This figure shows the topology of F_{16}CuPc deposited on 1D-microwires of TIPS-

pentacene [Fig. S3(a)] and in between the microwires [Fig. S3(b)]. Figures also show that the grain

sizes of the deposited F_{16}CuPc on 1D-microwires are smaller in comparison to the grain sizes

deposited in between 1D-microwires. The average and rms roughness of F_{16}CuPc film deposited on

1D-microwires are 0.875 and 1.105 nm, respectively. The average and rms roughness of F_{16}CuPc film

deposited in between the 1D-microwires are 0.921 and 1.161 nm, respectively.
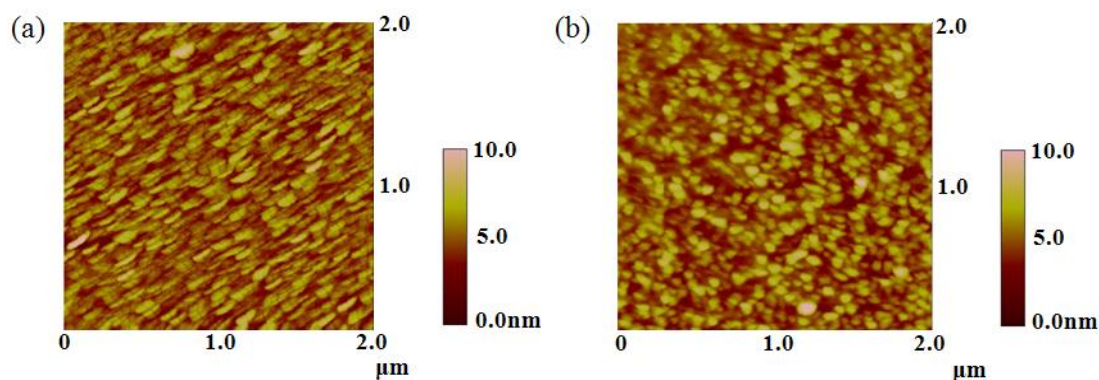
Fig. S3 (a) AFM images (2 x 2 μm^2).of $F_{16}CuPc$ film grown on 1D-microwires of TIPS-pentacene at 25 ^oC; (b) AFM images of $F_{16}CuPc$ film grown on polymer gate dielectric (in between the microwires) at 25 ^oC.
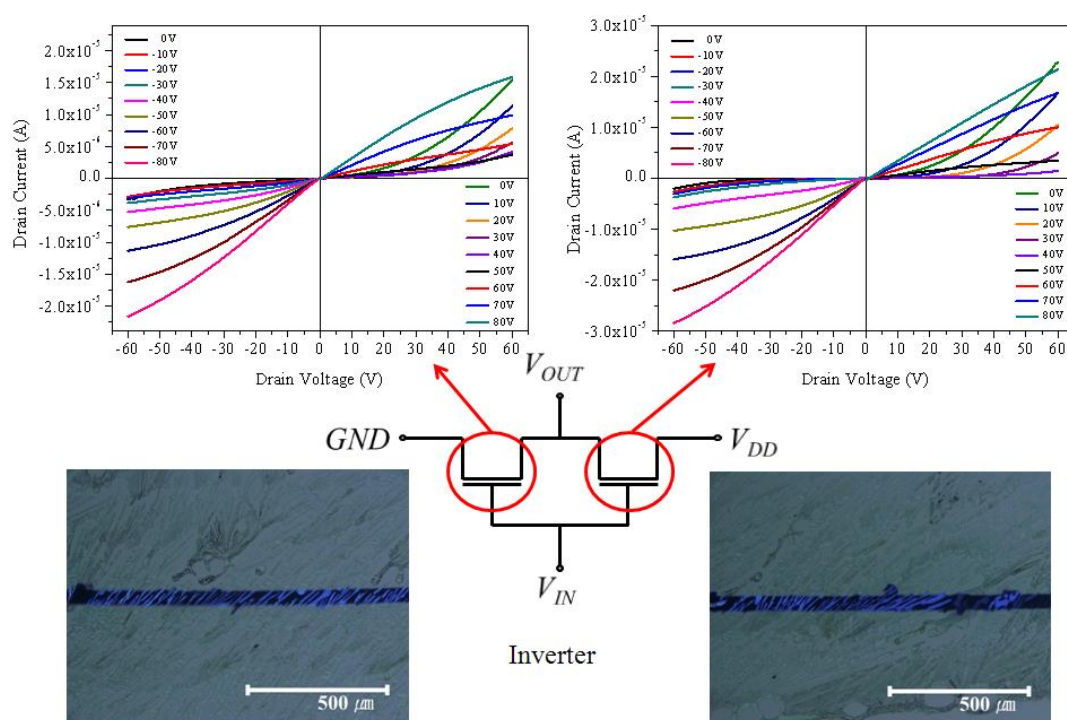
Fig. S4 Output curves of the CMOS-like inverter based on two ambi-OFETs based on alternating *p*- and *n*-channel along with the schematic diagram of the logic circuit and optical microscopic image of the channel region of both OFETs. Output characteristics of ambi-OFETs swept from V_{DS} 0 V to 60 V with an increment of 1 V with an applied constant V_{GS} from 0 V to 80 V (increment of 10 V).

Similarly, output characteristics of ambi-OFETs were measured by sweeping from V_{DS} 0 V to -60 V (increment of 1 V) with an applied constant V_{GS} from 0 V to -80 V (increment of -10 V).
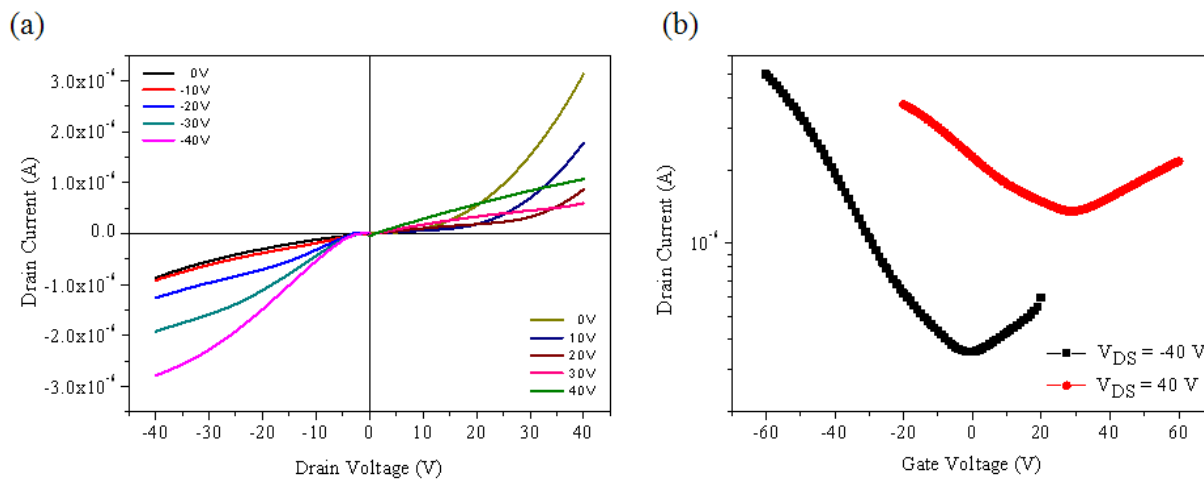
Fig. S5 (a) Output and (b) transfer characteristics of the ambi-OFET used in load type inverter.
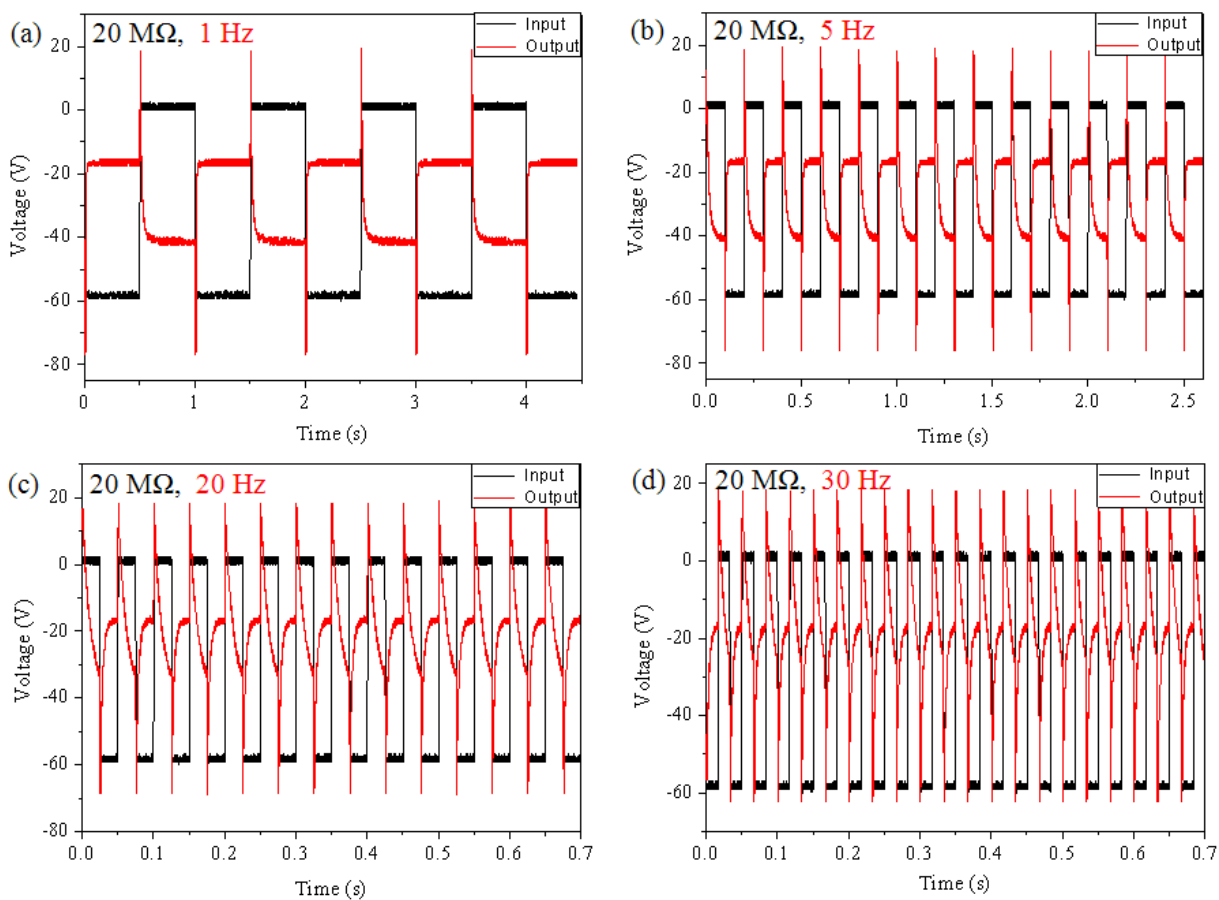
Fig. S6 The transient response of PMOS with a resistive load of 20 MΩ at constant drain bias when the gate voltage is pulsed at (a) 1 Hz, (b) 5 Hz, (c) 20 Hz and (d) 30 Hz.
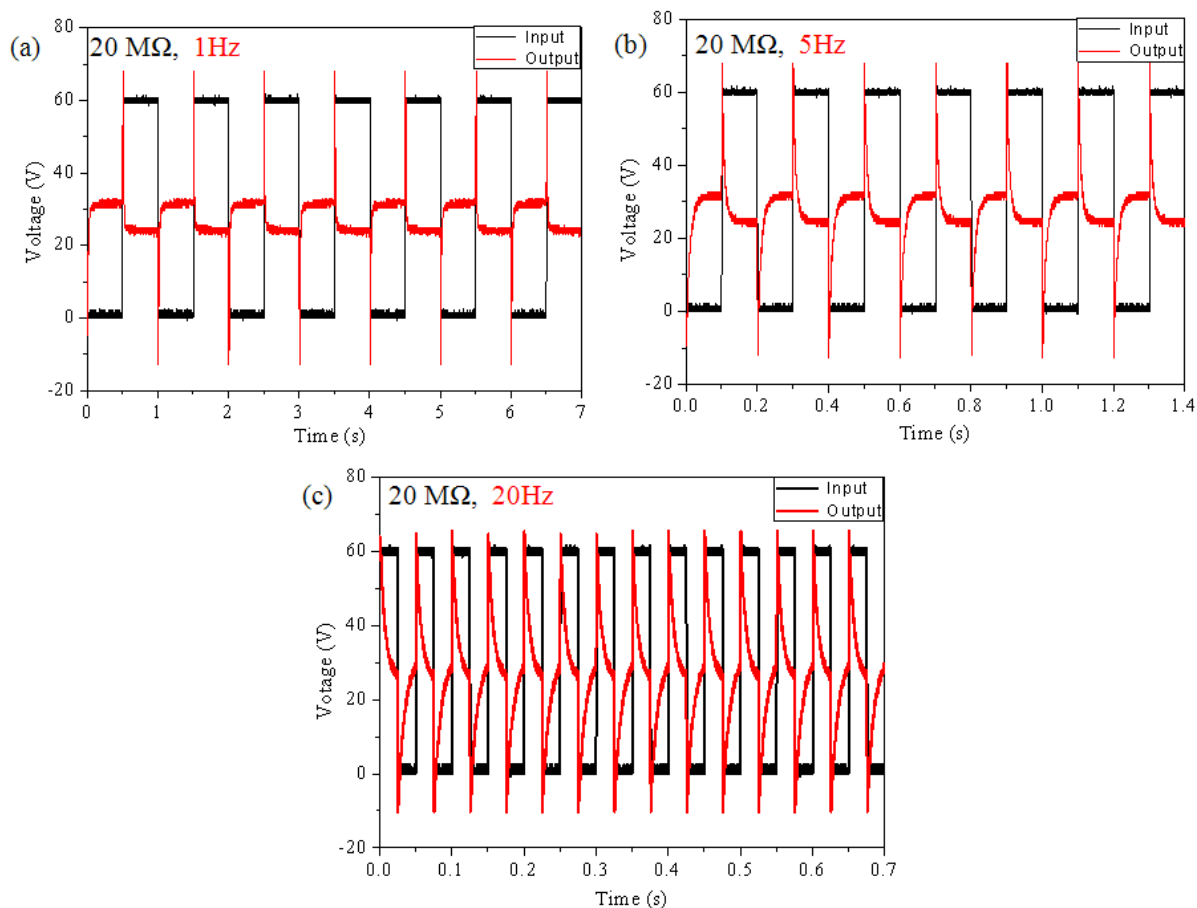
Fig. S7 The transient response of NMOS with a resistive load of 20 MΩ at constant drain bias when the gate voltage is pulsed at (a) 1 Hz, (b) 5 Hz, and (c) 20 Hz.